BioGecko

Vol 12 Issue 03 2023
ISSN NO: 2230-5807

A NEW DEEP LEARNING MODEL FOR THE CLASSIFICATION OF CROPS USING HYPERSPECTRAL DIGITAL DATA

S. Jamalaiah, Research Scholar
Department of Spatial Information Technology, Jawaharlal Nehru Technological University Hyderabad UCEST, Kukatpally, Hyderabad, India

K. Manjulavani, Professor
Department of Civil Engineering, Jawaharlal Nehru Technological University Hyderabad UCEST, Kukatpally, Hyderabad, India

ABSTRACT
Supervised classification of crops and crop identification are in the tillage area. Crop feature extraction and crop classification benefit greatly from the use of hyperspectral remote sensing data. Hyperspectral data is unstructured, and deep learning methods work well with unstructured data. In this research, customised 3-Dimensional convolutional neural network was used as a deep learning model and a study area dataset was obtained from the Airborne Visible InfraRed Imaging Spectrometer - Next Generation sensor for the extraction of crop features and crop classification. The case study has been conducted at the International Crops Research Institute for the Semi-Arid Tropics, Hyderabad, Telangana, India. The experiment shows that the customised 3-Dimensional convolutional neural network method achieves a good result with overall classification. When compared to other cutting-edge techniques, the overall accuracy of the study area is 99.50 percent.

Keywords: Classification, Convolutional Neural Network, Convolution, Deep Learning, Fully Connected, 3-Dimensional Convolutional Neural Network

INTRODUCTION

Images with a high spectral resolution are known as hyperspectral images. Which include more spectral data that can be used to understand and analyse spectrally comparable materials of interest [8]. Hyperspectral data were broadly used in land use land cover mapping, agricultural, mineralogy, physics, medical imaging, chemical imaging and environmental studies [7]. NASA's Jet Propulsion Laboratory (JPL) first proposed hyperspectral remote sensing in the early 1980s and it has since become an essential tool for remote sensing [6].

Crop identification and classification is an essential part of agricultural production. Crop classification and identification using hyperspectral remote sensing data is a difficult undertaking [7]. Classification and identification of crops using hyperspectral images are high dimensionality and spectrum mixing make this a difficult undertaking [23]. Barefaced computation and classification of the target and identification of crops imply more Low accuracy and high cost of computation [23]. Usually, hyperspectral data suffer with limitation of available labelled training samples. It is expensive and time-consuming to obtain these samples. A vast variety of classification methods to deal with hyperspectral data have been suggested in the time since the past decemvirate [14].

Because the scale issues, traditional classification algorithms (which can be divided into spectral-based and object-oriented methods) struggled to classify crops using hypespectral data [22]. Support vector machine (SVM), K-nearest neighbour (KNN), logistic regression (LR), and neural network (NN) are examples of traditional classification approaches that focus on the usage of spectral features. Due to noise

and other variables, the majority of these approaches result in low classification accuracy [2]. Many deep learning models have been used to classify and identify crops using hypespectral images in recent years. Stack auto encoder (SAE) [2], deep belief networks (DBN) [2], and CNN [10] are examples of classic deep learning models.

Related work

In recent past deep learning methods were very useful for the classification crops using hypespectral data. Many methods for hyperspectral image classification have been proposed in the literature. *Yulin Yan and Youngryel Ryu*, Leveraging Google Street View images, suggested a deep leaning method for crop type mapping [19]. To automatically categorise the Google Street View photos, the authors employed a convolutional neural network (CNN). The overall accuracy for identifying normal images was reported to be 92%. *Chunxing Wang et al.* A hyperspectral image classification approach based on a 3D CNN model was proposed [3]. The authors of this article use 3D CNN and J-M distance to classify hyperspectral images. In both datasets, the total accuracy for classifying different crops was reported to be 92.50 %. *Kavita Bhosle and Vijaya Musande*, CNN and convolutional auto encoder are two deep learning methods that have been suggested [7]. In this research, the authors used both methods to extract features before using Principal component analysis (PCA) to reduce dimensionality. Both methods are 90 % and 94% of the total accuracy, respectively. *Seyyed Ali Ahmadi and Nasser Mehrshad,* In this article on hyperspectral image classification, a Spectral-Spatial Feature Extraction (SEA-FE) approach was presented [13]. Spectral feature reduction using minimum noise fraction (MNF) is used in this method to obtain pixel feature maps, which are then used to compute SEAF. The hyperspectral image classification was found to have an overall accuracy of 92.13 %. *Xin Zhao et al.* For hyperspectral picture categorization, a multi-source deep learning method was proposed [18]. In this method, numerous hypespectral images are used to train a model, which is then applied to the target hyperspectral image. A 98.8% overall accuracy was reported for classifying target hyper spectral images. *Venkata Shashank Konduri et al.* proposed an approach to map a crop across the United States (USA) before harvest [16]. The first stage in crop classification in this approach was to build phenoregions using multivariate Spatio-Temporal clustering (MSTC). The next stage was to give each phenoregion a crop label based on the spatial agreement between phenoregions and crop. classes.*Yanfei Zhong et al*. presented a conditional random field classifier for a deep `convolutional neural network (CNNCRF) [21]. Crop categorization using unmanned aerial vehicles (UAV)-borne high spatial resolution images is presented in this framework. The overall accuracy of the WHU-Hi-Han Chuan dataset was 98.50%. *Jinfan Xu et al.* The Deep Crop Mapping (DCM) model, which is based on long short-term memory structure with attention mechanism, was developed through the integration of multi temporal and multi spectral remote sensing data [5]. This method gets 95% accuracy for crop classification. *Vishal Srivastava and Bhaskar Biswas*, For pixel classification in hyperspectral images, Deep CNN feature fusion, manifold learning, and regression are suggested [22]. The major goal of this project is to increase hyperspectral image categorization accuracy. This approach has a classification accuracy of 98.8%. *Ji Zhao et al.* presented a conditional random fields-based spectral-spatial agricultural crop mapping method (SCRF) [6]. It uses the spatial interaction of pixels to improve classification accuracy by learning the sensitive spectral information of crops using a spectrally weighted kernel. Overall crop classification accuracy was 88.24 %. *Liheng Zhong et al. provided a deep learning-based categorization framework for remotely observed time series data [9]*. This method classifies the summer crops using the land sat Enhanced Vegetation Index (EVI) time series. In this method, they design two deep learning models; one is Long Short-Term Memory (LSTM), and the other one is one-dimensional convolutional layers (conv1D). The highest accuracy (85.4%) was achieved

by the conv1D-based model. *Hongwei Zhao et al.* Three deep learning models for classifying early crops were proposed using Sentinel-1A time series data [4]. One-dimensional convolutional neural networks (1D-CNNs), long-short-term recurrent neural networks (LSTM RNNs), and gated recurrent recurrent neural networks are all used in deep learning models (GRU RNNs). For early crop classification, the most effective strategy combines all three models with an incremental classification method. This strategy offers a fresh look at early farmland mapping in overcast environments. *Shunping Ji et al.* For crop categorization, a novel 3-dimensional (3D) convolutional neural network (CNN) has been proposed [15]. Images from spatio-temporal remote sensing are used in this strategy. Using spatiotemporal remote sensing pictures, crop categorization accuracy was 79.4 %.

STUDY AREA

This research area of the **International Crops Research Institute for the Semi-Arid Tropics (ICRISAT)** can be found in Ranga Reddy district, Telangana state, India, located at 78.2752° E Longitude and 17.5111° N Latitude, covering an area of 500 hectares. The research location has semi-arid weather. The main crops grown in this area are sorghum, pearl millet, groundnuts, and chickpeas. When the data were collected, these crops had already been harvested. The research area map for ICRISAT is depicted in Figure 1.

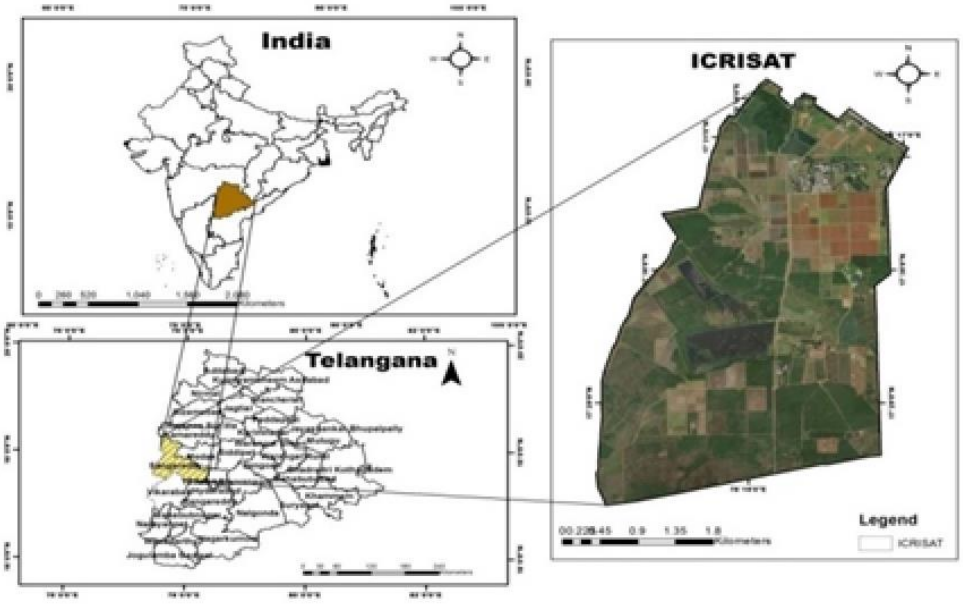

Figure 1. Study area map

Data

AVIRIS-NG Dataset of the ICRISAT study area

The Airborne Visible Infrared Imaging Spectrometer-Next Generation (AVIRIS-NG) was developed in collaboration with ISRO. It measures the wave length from 380nm to 2510nm with 5nm sampling. Spatial sampling is from 0.3m to 4.3m. The spectral resolution of data is 5nm to 0.5nm. The pixel size of the image is 27X27microns. The data resolution is 14 bits and the data rate is 74 bits per second. Figure 2

shows AVIRIS-NG data of the ICRISAT study area, data description shown in table 1, Obtained raw data from the NASA.gov website.

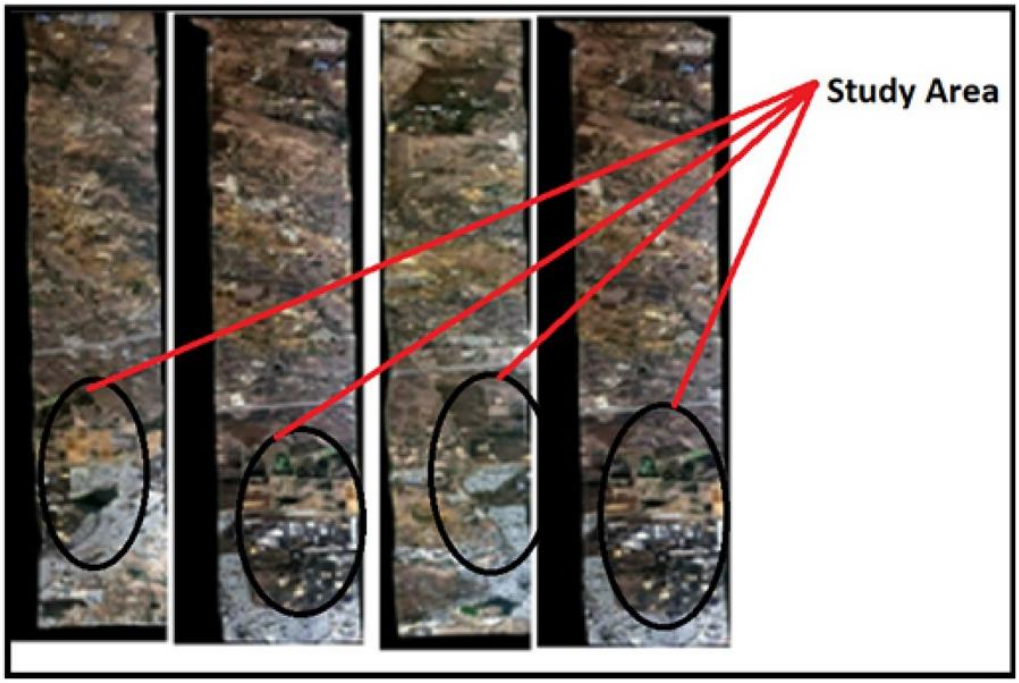

Figure 2. **AVIRIS–NG Data of study area.**

Table 1. Description of the study area data

Flight Name	Site Name	Investigator	Altitude (kft)	#Samples	# Lines	Pixel Size (meters)
ang20151219t081738	ICRISAT	ISRO,India	14.8	722	5592	4
ang20151219t082648	ICRISAT	ISRO, India	14.8	800	5697	4
ang20151219t083640	ICRISAT	ISRO, India	14.8	858	5668	4
ang20151219t084554	ICRISAT	ISRO, India	14.8	729	5762	4
ang20151219t080745	ICRISAT	ISRO, India	14.8	716	5665	4

METHODOLOGY

To classify hyperspectral images, a customised **3-Dimensional convolutional neural network (**3D-CNN) is used. This study focuses on pre-processing, image patching, and customising 3D-CNNs to classify AVIRIS-NG hyperspectral data. The Figure 3 demonstrates a novel deep learning model that uses hyperspectral digital data to classify crops.

The entire frame work includes three steps

1) Pre-Processing.
2) Image patching and splitting the samples.
3) Apply neural network model.

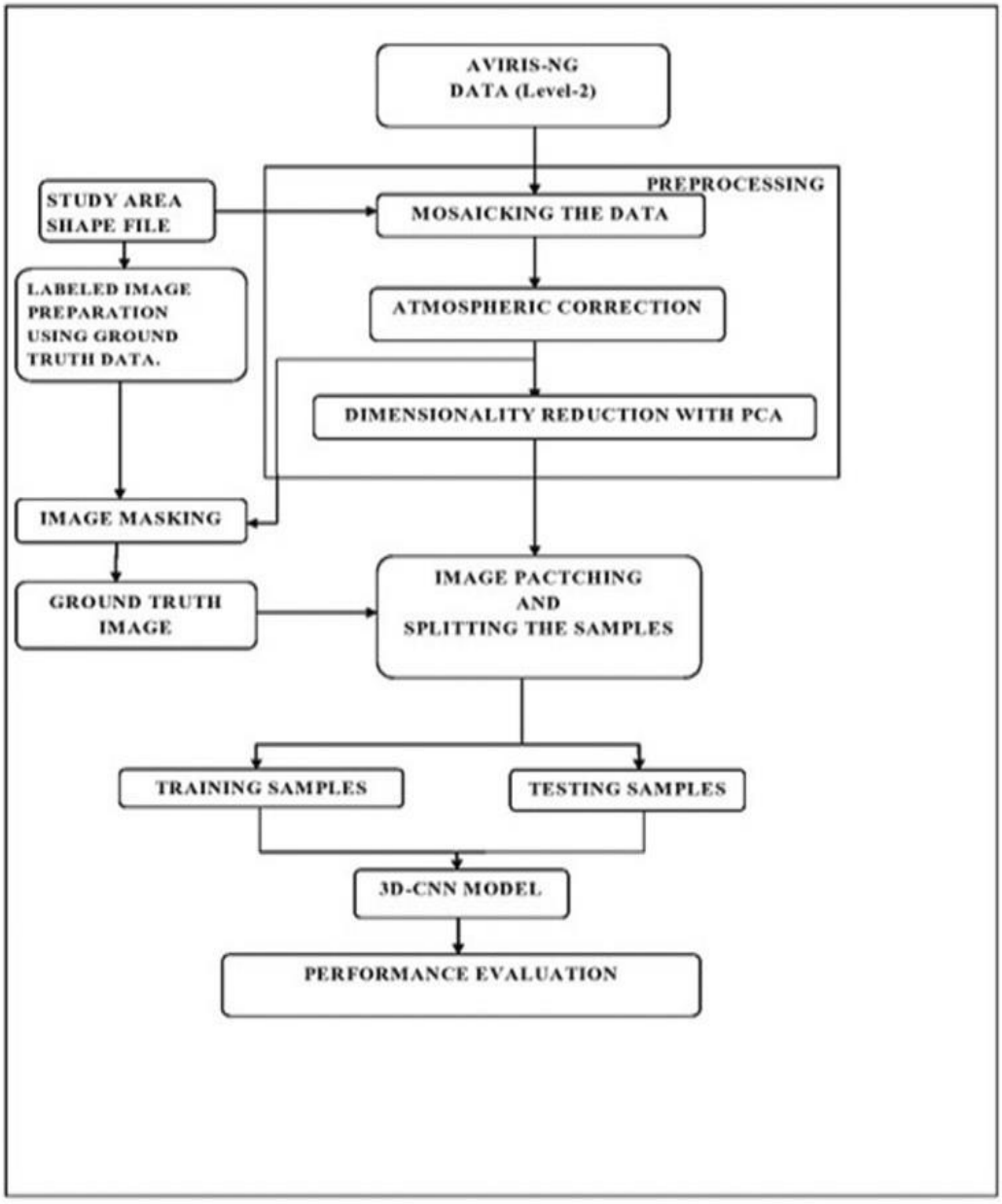

Figure 3. Flow chart of a new deep learning model for the classification of crops using hyperspectral digital data.

Figure 3. Flow chart of a new deep learning model for the classification of crops using hyperspectral digital data.

Pre-processing

Mosaic the Data

This entails integrating multiple images into a composite image. Envi software gives the potential for automated placement of georeferenced images in a georeferenced output mosaic. Figure 4 shows a mosaicked image using an ICRISAT boundary shape file.

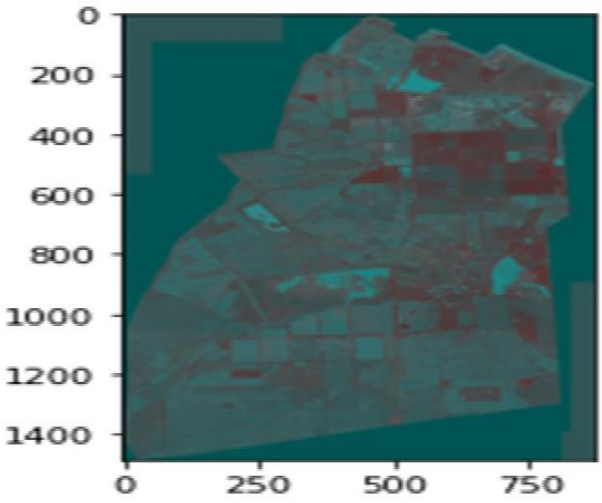

Figure 4.A mosaicked image using an ICRISAT border Shape file and raw data.

Atmospheric correction

The method of extracting surface reflectance from a remote sensing image by removing atmospheric effects is known as atmospheric correction. The removal of atmospheric effects on the reflectance values of the satellite image or airborne sensor image. Atmospheric correction has been shown to sufficiently improve accuracy. Atmospheric correction has four steps.

(1) Spectral features of the ground surface, direct measurements, and theatrical models are used to determine optical parameters of the atmosphere.
(2) Inversion procedures that derive surface reflectance can be used to rectify the remote sensing imaginary.
(3) Optical qualities of the atmosphere are approximated using theatrical models or spectral features of the ground surface.
(4) Inversion procedures that derive surface reflectance can be used to correct the remote sensing imaginary.

The atmospheric module provides two Atmospheric modelling tools for extracting spectral reflectance from the hyperspectral image.

(1) FLASH (Fast Line-of-sight Atmospheric Analysis of Spectral Hypercubes)
(2) QUAC (Quick atmospheric correction)

The QUAC and FLASS were developed by spectral sciences. Spectral science has been integral part in the development of Moderate resolution atmospheric Transmission (MODTRAN) atmospheric radiation transfer models. FLASH was the first tool that could correct wavelengths up to 300nm in the visible, near-infrared, and short-wave infrared regions. It only supports the band-interleaved-by-line (BIL) and band-interleaved-by-pixel (BIP) file formats, and the accuracy of the reflectance calculation is very low. Use the QUAC for this research. The Atmospheric Corrected Image of the ICRISAT Study Area is shown in Figure 5.

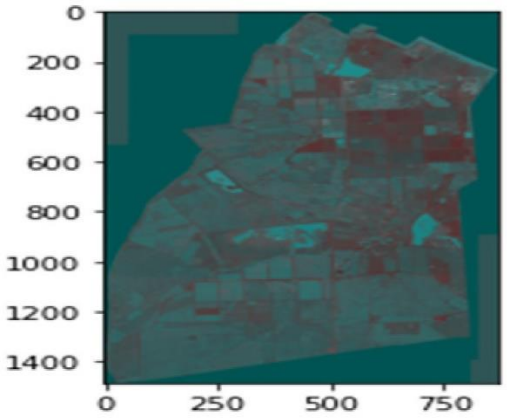

Figure 5. **Image with atmospheric correction.**

Label preparation

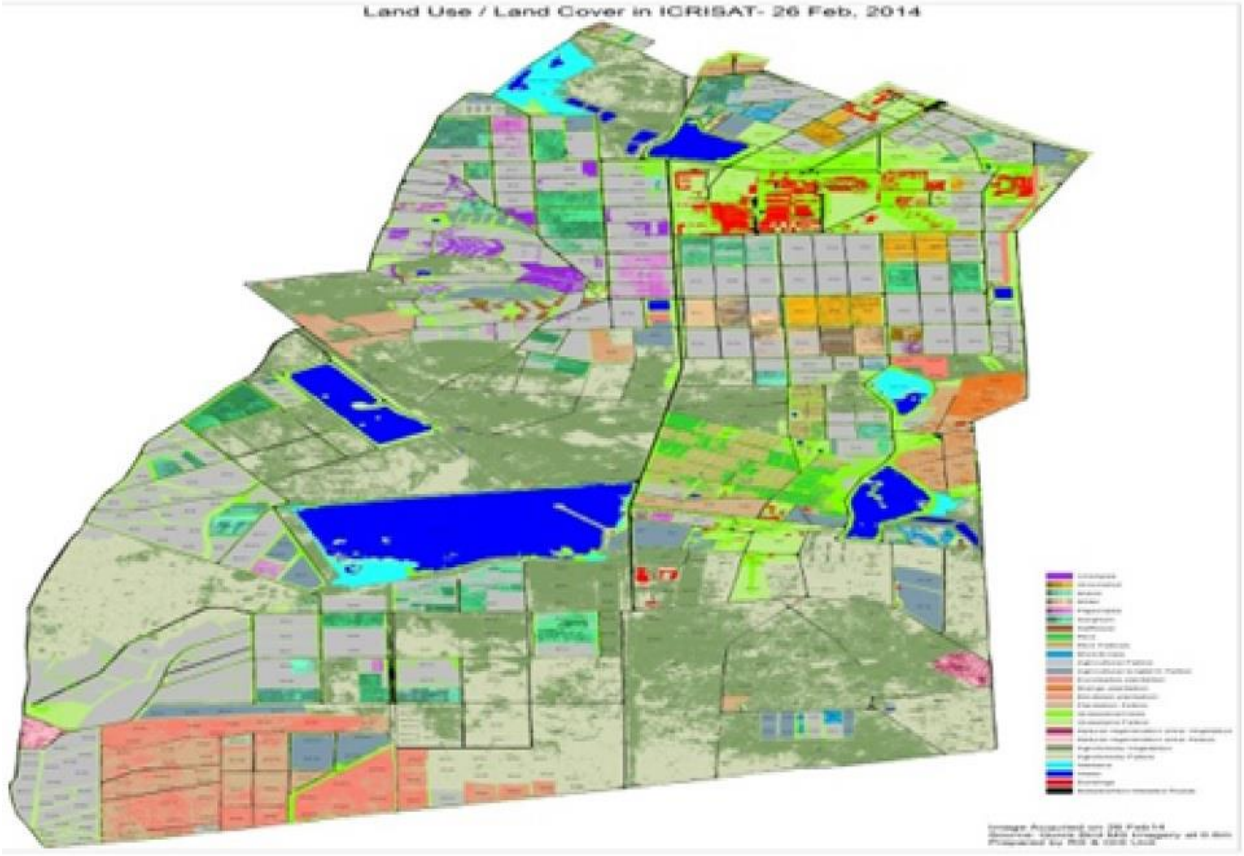

Figure 6. Land use land cover map of ICRISAT.

ICRISAT created the above land use and land cover map in 2014 using a Quick Bird multispectral image, down loaded from ICRISAT India website. This is used in this land use and land cover map used in this research for the preparation of labelled data for crop classification. In this research, Figure 6 and Google Earth Pro were used to determine the longitude and latitude of various crops in the study region, as indicated in Table 2.

Table 2. **Ground truth data for the ICRISAT study area.**

Class	Longitude	Latitude	Number of polygons
Sorghum	78º28’48.77“E	17º28’48.77“N	3
Rice	78º14’42.62“E	17º30’41.12“N	10
Millet	78º16’21.41“E	17º29’31.41“N	1
Mango plantation	78º16’45.61“E	17º29’48.72“N	1
Maize	78º16’01.17“E	17º28’58.78“N	4
Groundnut	78º16’03.30“E	17º30’19.00“N	17
Eucalyptus plantation	78º15’59.97“E	17º28’30.55“N	1
Chickpea	78º16’12.06“E	17º30’37.22“N	10
Built-up area	78º16’29.37“E	17º30’41.12“N	1
Boundary	78.2752º	17.5111º N	1

The labelled ground truth image shown in the Figure 7 was created using ground truth data and ArcGIS software.

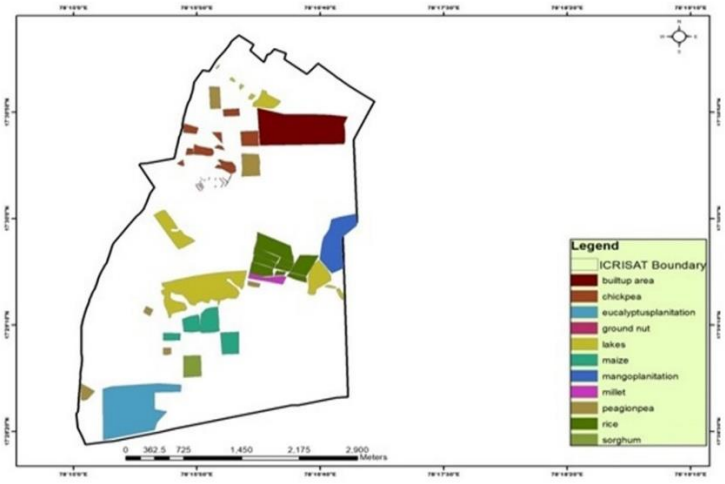

Figure 7. Labelled image using ground truth data.

Masking an image

This entails changing some of the image's pixel values to zero while leaving some pixels' values unchanged. The Image Masking tool uses an input image as a starting point, applies a mask to it, and then generates a new image that is a copy of the input image with the pixel intensity value set to zero or any other background intensity value, depending on the mask and masking operations carried out. Figure 8 shows a masked image using a shape file and ROIs. This image is used as a labelled image for supervised classification.

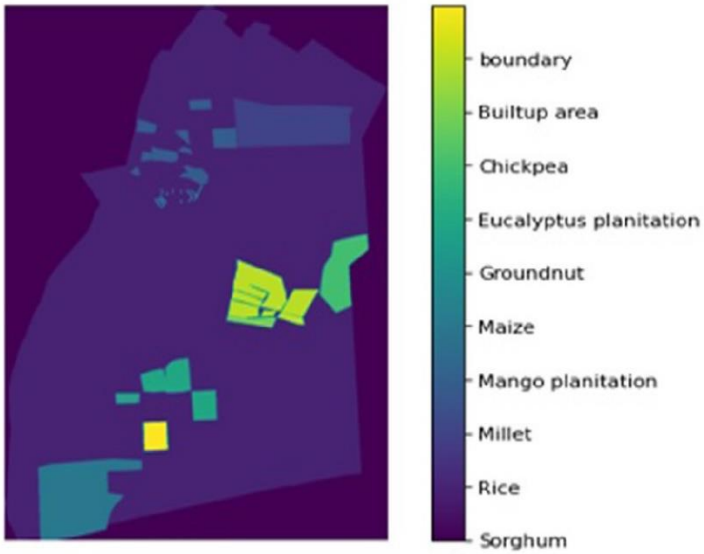

Figure 8. Masked image of using ground truth image, shape file, and ROIs

Dimensionality Reduction with PCA

Hyperspectral images have a high spectral correlation, resulting in redundant data. So, it is useful to reduce the dimensions in these images [2]. Dimensional reduction Figure 8. Masked image of using ground truth image, shape file, and ROIs

is the process of reducing features or dimensions of hyperspectral data and simplifies the subsequent process of classification. Principle component analysis is a transformation technique that can be utilised for dimensionality reduction of hyperspectral images. A large number of hyperspectral bands were analysed using kernel PCA to extract useful bands [3]. This paper proposes a reduction technique called principal component analysis (PCA). PCA is a very accepted method that is used to spectrally compact high-dimensional data sets [5], which selects the important bands for each pixel. Figure 9 show PCA for ICRISAT data sets. The plots show almost above 90% variance for the first 10 components of the ICRISAT dataset. Therefore, drop the other components.

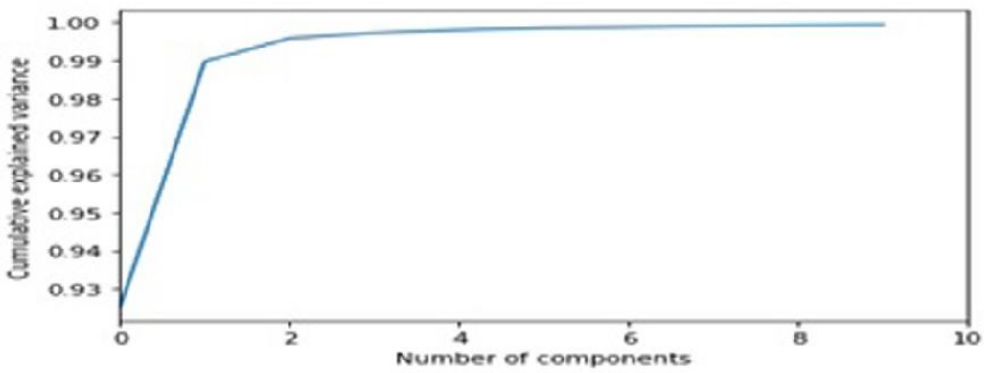

Figure 9. **PCA for ICRISAT data set.**

Apply neural network model

For classification and hyperspectral image feature extraction, CNN is the most frequently used method [23]. It offers good high-dimensional image processing capability, anticipative neural network architecture, artificial neurons that respond to a portion of the surrounding cells in the coverage region. There are two design ideas in convolution neural networks. The first is a correlated 2D structure of image pixels in nearby areas, and the second is a feature-sharing architecture. So, the generated feature map for each output through convolution uses the same filter in all locations [24].

Convolution neural network

There are four components to a convolutional neural network.

(1) Convolution layer
(2) Activation function
(3) Pooling layer
(4) Fully connected layer

Convolution layer

The convolution layer function is calculated from the following equation.

$a_j^k = \sum_{i=1}^{d} f(x_i^{k-1} * w_{ij}^k + b_j^k)$ (1)

Where matrix x_i^{k-1} is feature map of the $k-1$

Layer, a_j^k is a jth feature map of the kth layer, d represents the number of input feature maps, w_{ij}^k is the weight parameter and b_j^k is the bias parameter which is randomly initialized.

$f(x_i^{k-1} * w_{ij}^k + b_j^k)$ (2)

Is the nonlinear activation function where we are utilizing the ReLU activation function in this research.

* Is represents the convolution operation

Pooling layer

A pooling layer is commonly found immediately following the convolution layer. This is used to reduce the data's spatial dimension. A pooling operation reduces the network's parameters and prevents overfitting. The max-poling method is applied in this article.

Fully connected layer

The output value of each neuron in the connected layer is sent to the classifier after it interacts with all

neurons in the preceding layer. All of the parameters in the neural network are trained using the back-propagation algorithm. The CNN methods reused in the classification of hyperspectral images are 2-Dimensional-Convilutional Neural Network and 3-Dimensional-Convilutional Neural Network. In this proposed method, we are using 3D-CNN with PCA, 3D-CNN without PCA, and comparing both of them.

3D- Convolution neural network

3D- Convolution

From hyperspectral images, 3D-convolution extracts spectral and spatial information**.** (Chen et al., 2016). This can be computed by the below equation.

$$c_{abc} = f(\sum_{klm} w_{klm}\, a_{(x+k)(y+l)(z+m)} + b) \qquad (3)$$

Where the c_{abc} is the output feature at the position (a,b,c), $a_{(x+k)(y+l)(z+m)}$ represents input at the position (x+k, y+l, z+m) in which (k,l,m) denotes in its offset to (a, b, c) and w_{klm} weighted for the input. $a_{(x+k)(y+l)(z+m)}$ With an offset of (k, l, m) in the convolution kernel the feature size is smaller.

The Rectifier linear unit activation

The Rectifier linear unit (ReLU) is a nonlinear function that operates in a nonlinear manner. If a neuron's input is positive, the ReLU accepts it; if the input is negative, it returns zero. The features of the ReLU activation function are rapid gradient progression, sparse activation, and minimal computing effort [6].

$$f(x) = \max(0, x) \qquad (4)$$

Where x is input data,

ReLU in 3D-CNN can improve the performance in the large majority of applications.

Proposed 3D-Convolution network model

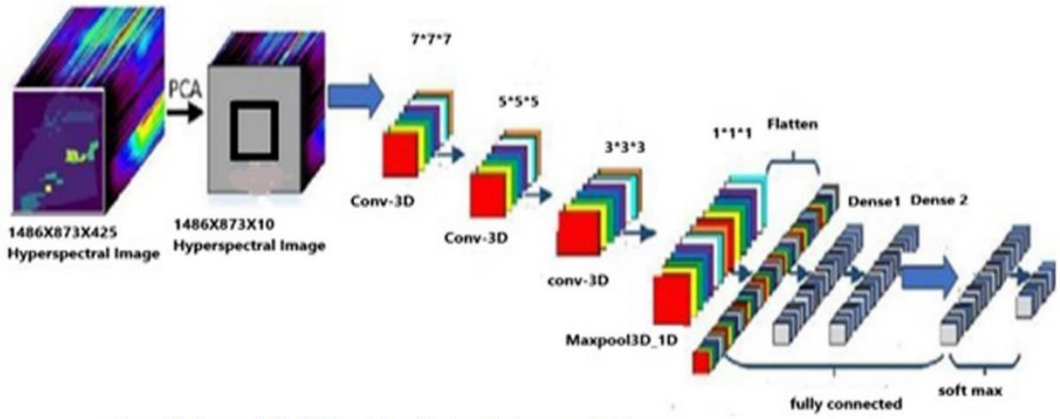

Figure 10. **Proposed 3D-CNN model architecture for hyperspectral images.**

Figure 10 shows the proposed 3D-CNN model for hyperspectral images. This model first uses the PCA for the reduction of data and then its reduced input to the proposed network model to extract features at different levels of layers, such as convolution layers, Max_pooling layers, and dense layers. Finally, classification is performed on fully connected layers and softmax functions. The number of fully connected layers and 3D convectional layers can be referred to in table.3 and table.4 for two datasets.

Table 3. **Network topology of the proposed 3D-CNN model architecture with window size:** 11×11 pixels.

Layer	Output shape	# parameters
Input Layer	(11, 11,50,1)	0
conv3d_1 (3D convolution layer)	(9, 9, 48, 16)	448
conv3d_2 (3D convolution layer)	(7, 7, 46, 32)	13856
conv3d_3(3D convolution layer)	(5, 5, 44, 64)	55360
max_pooling3d_1 (MaxPooling layer)	(2, 2, 22, 64)	0
flatten (Flatten)	(5632)	0
dense -1(Dense)	(512)	2884096
dense_2 (Dense)	(#classes)	8208
In total ,2,961,968 trainble prameters are required		

Table 4. Network topology of the proposed 3D-CNN model architecture with window size: 9×9 pixels.

Layer	Output shape	#parameters
Input Layer	(9, 9,50,1)	0
conv3d_1 (3D convolution layer)	(7, 7, 8, 16)	448
conv3d_2 (3D convolution layer)	(5, 5, 6, 32)	13856
conv3d_3(3D convolution layer)	(3, 3, 4, 64)	55360
max_pooling3d (MaxPooling layer)	(1, 1, 2, 64)	0
flatten (Flatten layer)-1	(128)	0
flatten(Flatten layer)-2	(128)	0
dense_1 (Dense layer)	(#classes)	4617
In total 1,40,842 trainble prameters are required		

RESULTS AND DISCUSSIONS

To use the proposed 3D-CNN to classify different crops, 75% of each class's samples are selected as training samples, with the remaining samples being used as testing samples. All experiments were implemented by using Python 3 with Anaconda's environment. In the customized 3D-CNN model network contain three 3D-convolutional layers, one max-pooling layer, two dense layers and one fully

connected layer. To perform a fair comparison for all experiments with a learning rate of 0.001, an activation function Relu is used for all except the last layer with softmax, and 9×9×10 pixels and 11×11×10 pixels for the ICRISAT data set, respectively. The 10 bands are selected by using the PCA method. For the purpose of evolution, when comparing and analysing the results of crop classification, the confusion matrix made up of the true pixel and true pixel classification was used to calculate the average accuracy (AA), overall accuracy (OA), and Kappa coefficient (K). Figure 11 show the confusion matrix of ICRISAT datasets.

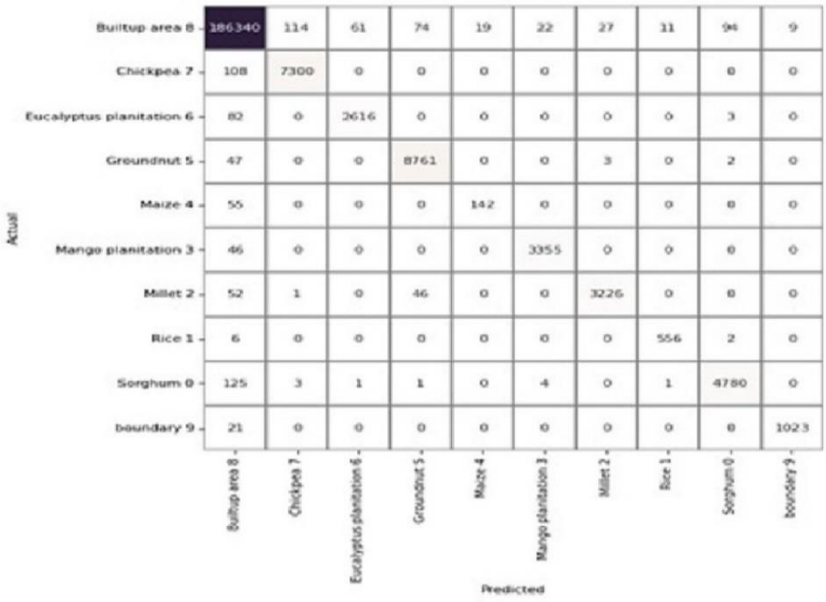

Figure 11. The Confusion Matrix for ICRISAT datasets.

The average class-wise classification is presented by the average accuracy, the number of correctly classified samples out of a total number of samples is calculated using the overall accuracy. And finally, the kappa coefficient indicates a high level of agreement between the classification and ground truth maps. The statistical metric is called the kappa coefficient. F1-score, precision, and support all evolved into AA, OA, and Kappa. Figure 12 show the convergence of accuracy and loss of our proposed 3D-CNN for 500 epochs with PCA of both datasets.

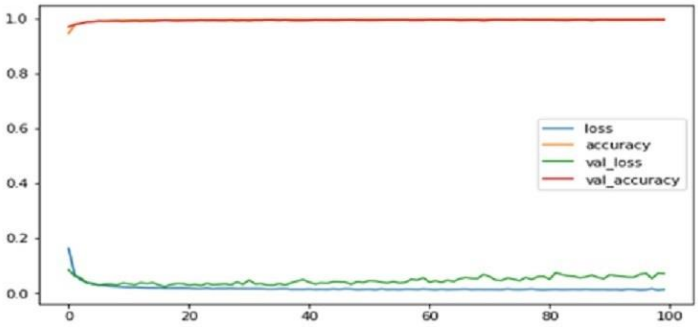

Figure 12. Proposed 3D-CNN model's accuracy and loss on the ICRISAT dataset.

The computational time is shown in table 5, and the computational time depends on the available RAM.

Table 5. The computation time of the ICRISAT dataset

Dataset	Computation Time (Minutes)
ICRISAT	0.5

Tables 6, provide the detailed classification of each class in the ICRISAT datasets with different window sizes. Figure 13 shows the detailed class accuracy comparison of the ICRISAT dataset.

Table 6. Detailed accuracy of the ICRISAT dataset

Class Number	Class Name	Accuracy (%)	
		Window size:9×9 pixels	Window size:11×11 pixels
1	Sorghum	99.76	99.93
2	Rice	98.54	98.97
3	Millet	96.85	96.72
4	Mango plantation	99.40	99.32
5	Maize	97.02.	97
6	Groundnut	98.58	98.45
7	Eucalyptus plantation	97.25	96.45
8	Chickpea	97.98	97.92
Test Accuracy		**99.52**	**99.49**
Overall Accuracy		**99.52**	**99.49**
Average accuracy		**95.60**	**95.52**
Kappa		**98.23**	**98.19**

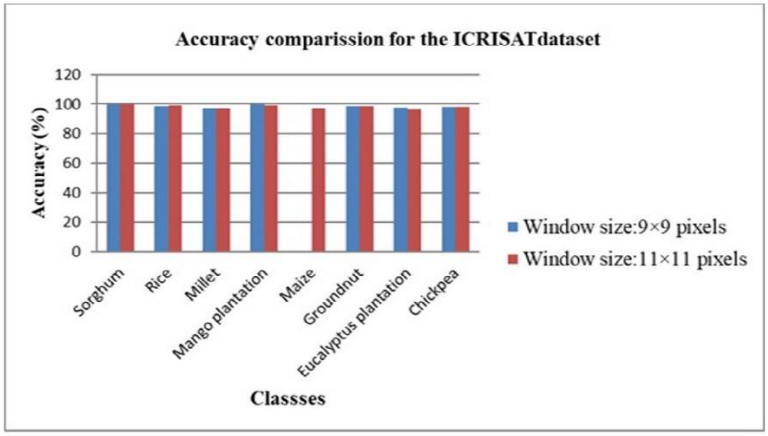

Figure 13. **Comparison of detail class accuracy for ICRISAT dataset.**

Generally, the proposed deep learning model always achieves classification images that visually much more similar to the original hyperspectral images with no noise. Figure 14 and Figure 15 are shows the classification images and Ground truth images with different window sizes of ICRISAT dataset.

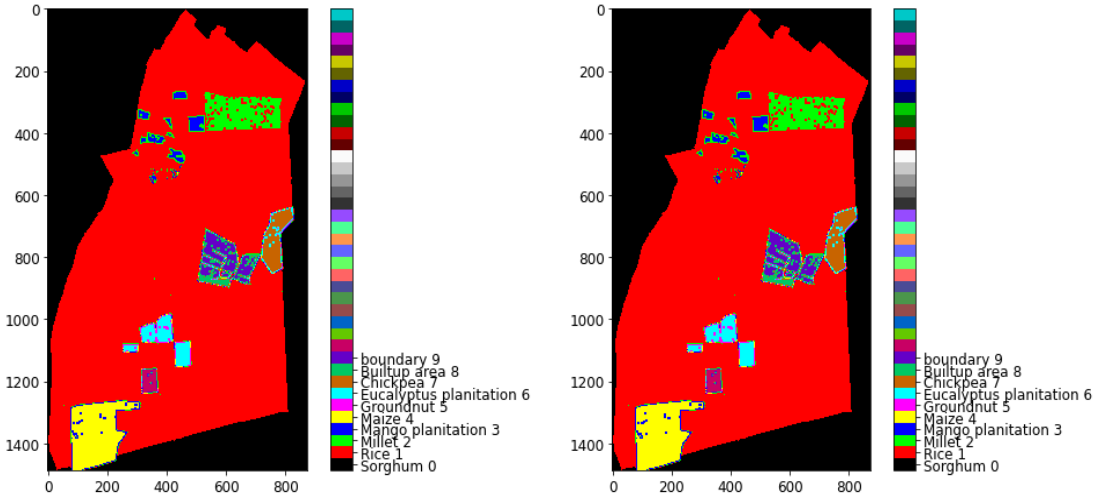

(a) (b)

Fig.18.Classification image of the ICRISAT dataset. (a) window size: 9×9 and (b) window size: 11×11 pixels.

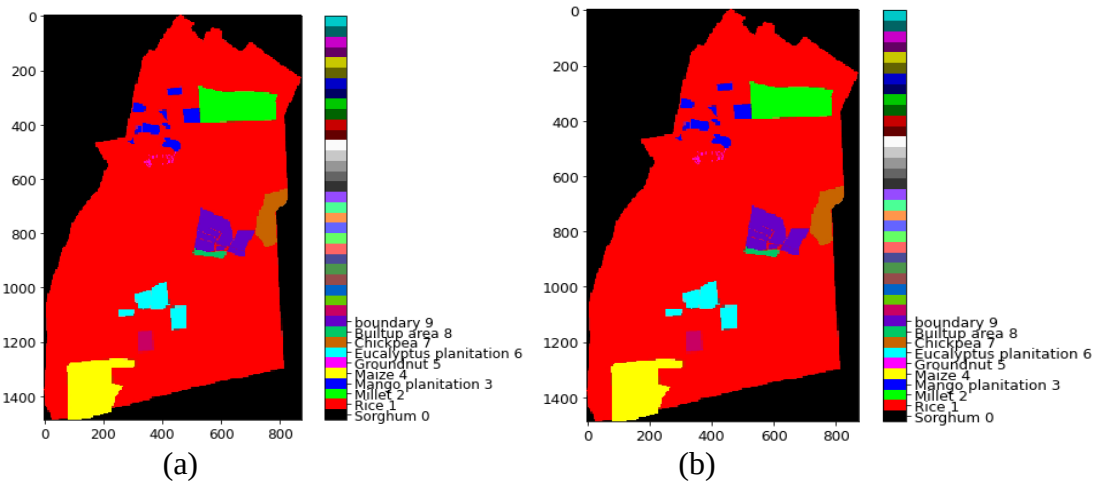

(a) (b)

Ground truth image of ICRISAT dataset. (a) window size: 9×9 pixels and (b) window size: 11×11 pixels.

CONCLUSIONS AND FUTURE SCOPE

The deep learning method (DLM) for classifying crops using hyperspectral digital data was developed and validated in this work. It also used two datasets for the DLM and also used a customized 3D-CNN. 75% of samples in the ICRISAT dataset are selected as training samples, with the remaining 25% selected as testing samples for ICRISAT dataset. Calculations for the evolution's AA, OA, and K were made using the confusion matrix. On both datasets, the overall classification accuracy may be significantly increased with the modified 3D-CNN. The average accuracy, over-all accuracy, and kappa coefficient of the ICRISAT dataset are 95.60%, 99.52%, and 98.23%. The computational times for all experiments in the ICRISAT dataset are 0.56 minutes. Furthermore, the model of deep learning is used for crop health

detection.

Interest-based conflict

The authors declare no conflict of Interest

contributions from author

Mr.S.Jamalaiah conducts the research and wrote the paper; Prof..K.Manjulavani guides the research; Both authors had approved the final version.

REFERENCES

Bishir, M. *et al.* (2020) 'Sleep Deprivation and Neurological Disorders', *BioMed research international*, 2020, p. 5764017.

Bodner, L., Woldenberg, Y. and Bar-Ziv, J. (2003) 'Radiographic features of large cystic lesions of the jaws in children', *Pediatric radiology*, 33(1), pp. 3–6.

Boyczuk, M. P., Berger, J. R. and Lazow, S. K. (1995) 'Identifying a deciduous dentigerous cyst', *Journal of the American Dental Association* , 126(5), pp. 643–644.

Chandrasekar, R. *et al.* (2020) 'Development and validation of a formula for objective assessment of cervical vertebral bone age', *Progress in orthodontics*, 21(1), p. 38.

Delbem, A. C. B. *et al.* (2006) 'Dentigerous cysts in primary dentition: report of 2 cases', *Pediatric dentistry*, 28(3), pp. 269–272.

Fan, Y. *et al.* (2021) 'Tomentosin Reduces Behavior Deficits and Neuroinflammatory Response in MPTP-Induced Parkinson's Disease in Mice', *Journal of environmental pathology, toxicology and oncology: official organ of the International Society for Environmental Toxicology and Cancer*, 40(1), pp. 75–84.

Felicita, A. S. and Sumathi Felicita, A. (2018) 'Orthodontic extrusion of Ellis Class VIII fracture of maxillary lateral incisor – The sling shot method', *The Saudi Dental Journal*, pp. 265–269. doi: 10.1016/j.sdentj.2018.05.001.

Gan, H. *et al.* (2019) 'Zingerone induced caspase-dependent apoptosis in MCF-7 cells and prevents 7,12-dimethylbenz(a)anthracene-induced mammary carcinogenesis in experimental rats', *Journal of biochemical and molecular toxicology*, 33(10), p. e22387.

Iatrou, I., Theologie-Lygidakis, N. and Leventis, M. (2009) 'Intraosseous cystic lesions of the jaws in children: a retrospective analysis of 47 consecutive cases', *Oral surgery, oral medicine, oral pathology, oral radiology, and endodontics*, 107(4), pp. 485–492.

Jones, A. V., Craig, G. T. and Franklin, C. D. (2006) 'Range and demographics of odontogenic cysts diagnosed in a UK population over a 30-year period', *Journal of oral pathology & medicine: official publication of the International Association of Oral Pathologists and the American Academy of Oral Pathology*, 35(8), pp. 500–507.

J, P. C. *et al.* (2018) 'Prevalence and measurement of anterior loop of the mandibular canal using CBCT: A cross sectional study', *Clinical Implant Dentistry and Related Research*, pp. 531–534. doi: 10.1111/cid.12609.

Li, S. *et al.* (2019) 'Restorative Effect of Fucoxanthin in an Ovalbumin-Induced Allergic Rhinitis Animal Model through NF-κB p65 and STAT3 Signaling', *Journal of environmental pathology, toxicology and oncology: official organ of the International Society for Environmental Toxicology and Cancer*, 38(4), pp. 365–375.

Manor, E. *et al.* (2012) 'Cystic Lesions of the Jaws - A Clinicopathological Study of 322 Cases and Review of the Literature', *International Journal of Medical Sciences*, pp. 20–26. doi: 10.7150/ijms.9.20.

Martínez-Pérez, D. and Varela-Morales, M. (2001) 'Conservative treatment of dentigerous cysts in children: A report of 4 cases', *Journal of Oral and Maxillofacial Surgery*, pp. 331–333. doi: 10.1053/joms.2001.21006.

Ma, Y. *et al.* (2019) 'Sesame Inhibits Cell Proliferation and Induces Apoptosis through Inhibition of STAT-3 Translocation in Thyroid Cancer Cell Lines (FTC-133)', *Biotechnology and bioprocess engineering: BBE*, 24(4), pp. 646–652.

Meara, J. G. *et al.* (1996) 'Odontogenic Keratocysts in the Pediatric Population', *Archives of Otolaryngology - Head and Neck Surgery*, pp. 725–728. doi: 10.1001/archotol.1996.01890190021006.

Miyawaki, S. *et al.* (1999) 'Eruption speed and rate of angulation change of a cyst-associated mandibular second premolar after marsupialization of a dentigerous cyst', *American journal of orthodontics and dentofacial*

orthopedics: official publication of the American Association of Orthodontists, its constituent societies, and the American Board of Orthodontics, 116(5), pp. 578–584.
Mudigonda, S. K. *et al.* (2020) 'Non-suturing microvascular anastomosis in maxillofacial reconstruction- a comparative study', *Journal of Cranio-Maxillofacial Surgery*, 48(6), pp. 599– 606.
Murakami, A. *et al.* (1995) 'Eruption of an impacted second premolar after marsupialization of a large dentigerous cyst: case report', *Pediatric dentistry*, 17(5), pp. 372–374.
Narayanasamy, R. K. *et al.* (2021) 'Lower pretreatment hemoglobin status and treatment breaks in locally advanced head and neck squamous cell carcinoma during concurrent chemoradiation', *Indian journal of cancer*, 58(1), pp. 62–68.
'Oral pathology: Clinical pathologic correlations (ed 3)' (1999) *Journal of Oral and Maxillofacial Surgery*, pp. 633–634. doi: 10.1016/s0278-2391(99)90110-6.
Prabhu, N. T., Rebecca, J. and Munshi, A. K. (1996) 'Dentigerous cyst with inflammatory etiology from a deciduous predecessor--report of a case', *Journal of the Indian Society of Pedodontics and Preventive Dentistry*, 14(2), pp. 49–51.
Ramakrishnan, M., Dhanalakshmi, R. and Subramanian, E. M. G. (2019) 'Survival rate of different fixed posterior space maintainers used in Paediatric Dentistry – A systematic review', *The Saudi Dental Journal*, pp. 165–172. doi: 10.1016/j.sdentj.2019.02.037.
Rubin, D. M., Vedrenne, D. and Portnof, J. E. (2002) 'Orthodontically guided eruption of mandibular second premolar following enucleation of an inflammatory cyst: case report', *The Journal of clinical pediatric dentistry*, 27(1), pp. 19–23.
Saravanakumar, K. *et al.* (2021) 'Chemical composition, antioxidant, and anti-diabetic activities of ethyl acetate fraction of Stachys riederi var. japonica (Miq.) in streptozotocin-induced type 2 diabetic mice', *Food and chemical toxicology: an international journal published for the British Industrial Biological Research Association*, 155, p. 112374.
Sathya, S. *et al.* (2020) 'An in vitro study on hexavalent chromium [Cr(VI)] remediation using iron oxide nanoparticles based beads', *Environmental Nanotechnology, Monitoring & Management*, 14, p. 100333.
Scholl, R. J. *et al.* (1999) 'Cysts and Cystic Lesions of the Mandible: Clinical and Radiologic- Histopathologic Review', *Radio Graphics*, pp.1107–1124.doi: 10.1148/radiographics.19.5.g99se021107.
Stoelinga, P. J. (2001) 'Long-term follow-up on keratocysts treated according to a defined protocol', *International journal of oral and maxillofacial surgery*, 30(1), pp. 14–25.
Su, P. *et al.* (2019) 'A ginger derivative, zingerone-a phenolic compound-induces ROS-mediated apoptosis in colon cancer cells (HCT-116)', *Journal of biochemical and molecular toxicology*, 33(12), p. e22403.
Veeraraghavan, V. P. *et al.* (2021) 'A Comprehensive and Critical Review on Ethnopharmacological Importance of Desert Truffles: Terfezia claveryi, Terfezia boudieri, and Tirmania nivea', *Food Reviews International*, pp. 1–20.
Wahab, P. U. A. *et al.* (2018) 'Scalpel Versus Diathermy in Wound Healing After Mucosal Incisions: A Split-Mouth Study', *Journal of oral and maxillofacial surgery: official journal of the American Association of Oral and Maxillofacial Surgeons*, 76(6), pp. 1160–1164.
Wang, H. *et al.* (2021) 'Phyllanthin inhibits MOLT-4 leukemic cancer cell growth and induces apoptosis through the inhibition of AKT and JNK signaling pathway', *Journal of biochemical and molecular toxicology*, 35(6), pp. 1–10.
Wan, J. *et al.* (2020) 'Antiatherosclerotic Activity of Eriocitrin in High-Fat-Diet-Induced Atherosclerosis Model Rats', *Journal of environmental pathology, toxicology and oncology: official organ of the International Society for Environmental Toxicology and Cancer*, 39(1), pp. 61–75.
Weber, A. L. (1993) 'Imaging of cysts and odontogenic tumors of the jaw. Definition and classification', *Radiologic clinics of North America*, 31(1), pp. 101–120.
Wei, W. *et al.* (2021) 'Amelioration of oxidative stress, inflammation and tumor promotion by Tin oxide-Sodium alginate-Polyethylene glycol-Allyl isothiocyanate nanocomposites on the 1,2- Dimethylhydrazine induced colon carcinogenesis in rats', *Arabian Journal of Chemistry*, 14(8), p. 103238.

Young, C. W., Pogrel, M. A. and Schmidt, B. L. (2007) 'Quality of life in patients undergoing segmental mandibular resection and staged reconstruction with nonvascularized bone grafts', *Journal of oral and maxillofacial surgery: official journal of the American Association of Oral and Maxillofacial Surgeons*, 65(4), pp. 706–712.

Zhang, C. *et al.* (2020) 'Vicenin-2 Treatment Attenuated the Diethylnitrosamine-Induced Liver Carcinoma and Oxidative Stress through Increased Apoptotic Protein Expression in Experimental Rats', *Journal of environmental pathology, toxicology and oncology: official organ of the International Society for Environmental Toxicology and Cancer*, 39(2), pp. 113– 123.